J. Fluid Mech. (2016), *vol.* 794, *pp.* 444–459.
doi:10.1017/jfm.2016.174

A local analysis of the axisymmetric Navier–Stokes flow near a saddle point and no-slip flat boundary

P.-Y. Hsu[1,†], **H. Notsu**[2] **and T. Yoneda**[3]

[1]Graduate School of Mathematical Sciences, University of Tokyo, 3-8-1 Komaba, Meguro-ku, Tokyo 153-8914, Japan

[2]Waseda Institute for Advanced Study, Waseda University, 3-4-1 Ohkubo, Shinjuku-ku, Tokyo 169-8555, Japan

[3]Department of Mathematics, Tokyo Institute of Technology, Meguro-ku, Tokyo 152-8551, Japan

(Received 11 May 2015; revised 4 January 2016; accepted 1 March 2016)

Tornadoes are one type of violent flow phenomenon and occur in many places in the world. There are many research methods that aim to reduce the loss of human lives and material damage caused by tornadoes. One effective method is numerical simulation such as that in Ishihara *et al.* (*J. Wind Engng Ind. Aerodyn.*, vol. 99, 2011, pp. 239–248). The swirling structure of the Navier–Stokes flow is significant for both the mathematical analysis and numerical simulations of tornadoes. In this paper, we try to clarify the swirling structure. More precisely, we performed numerical computations on axisymmetric Navier–Stokes flows with a no-slip flat boundary. We compared a hyperbolic flow with swirl and one without swirl, and observed that the following phenomenon occurs only in the swirl case: the distance between the point with the maximum magnitude of velocity $|\boldsymbol{v}|$ and the z-axis changed drastically at a specific time (which we call the turning point). Besides, an 'increasing velocity phenomenon' occurred near the boundary, and the maximum value of $|\boldsymbol{v}|$ was obtained near the axis of symmetry and the boundary when the time was close to the turning point in the swirl case.

Key words: mathematical foundations, Navier–Stokes equations

1. Introduction

In this study we considered the local behaviour of the three-dimensional (3D) Navier–Stokes flow near a saddle point (with hyperbolic flow configuration) and no-slip flat boundary. The Navier–Stokes equations with no-slip flat boundary are expressed as

$$\left.\begin{aligned} &\partial_t \boldsymbol{v} + (\boldsymbol{v}\cdot\nabla)\boldsymbol{v} - \nu\Delta\boldsymbol{v} + \nabla p = 0 \quad \text{in } \mathbb{R}^3_+ \times [0,T), \\ &\boldsymbol{v_0} = \boldsymbol{v}|_{t=0}, \quad \boldsymbol{v}|_{\partial\mathbb{R}^3_+} = 0, \quad \nabla\cdot\boldsymbol{v} = 0 \quad \text{in } \mathbb{R}^3_+ \times [0,T), \end{aligned}\right\} \tag{1.1}$$

† Email address for correspondence: pyhsu@ms.u-tokyo.ac.jp

where $\boldsymbol{v}$ is a vector field representing the velocity of the fluid, and p is the pressure. We will use bold to denote vector-valued functions throughout this paper. The term 'hyperbolic flow configuration' used hereafter can be defined in cylindrical polar coordinates as follows: there is $\delta > 0$ (depending on t) such that $v_z > 0$, $v_r < 0$, or $v_z < 0$, $v_r > 0$ for $0 < r < \delta$ and $0 < z < \delta$, where v_z and v_r represent the axial and radial components of velocity $\boldsymbol{v}$. A simple modification is required for defining a two-dimensional (2D) hyperbolic flow configuration.

Recently, the Euler flow with a saddle point (with hyperbolic flow configuration) has been extensively studied. Bourgain & Li (2015*a*) obtained strong local ill-posedness results in the Sobolev spaces $W^{n/p+1,p}$ for any $1 < p < \infty$ and in the Besov spaces $B^{n/p+1}_{p,q}$ with $1 < p < \infty$ and $1 < q \leqslant \infty$ and $n = 2$ or 3 by using a combination of Lagrangian and Eulerian techniques with a saddle point (with hyperbolic flow configuration) structure. In particular, they settled the borderline Sobolev case $H^{n/2+1}$. After that Elgindi & Masmoudi (2014) and Bourgain & Li (2015*b*) produced similar results for the C^1 case (also the C^m case). On the other hand, Kiselev & Sverak (2014) (also refer to Itoh, Miura & Yoneda (2014), Kiselev & Zlatos (2015) and Xu (2014) for related topics) showed a 2D Euler flow with a saddle point (with hyperbolic flow configuration) in a disk for which the gradient of vorticity exhibited a double-exponential growth in time for all times. Their estimate is known to be sharp, namely, the double-exponential growth is the fastest possible growth rate. These results show that the saddle point (with hyperbolic flow configuration) causes some type of unstabilizing effects.

In the next part of § 1, for the convenience of readers belonging to different research fields, the related results are organized as follows. First, we introduce results obtained from mathematical analysis, and then discuss the research on tornado-like vortices. Finally, we provide several references of related literature in each research field (mathematical analysis, numerical analysis and research on tornadoes) for the convenience of readers.

In the following four paragraphs, we introduce classical regularity results and a new regularity criterion on the direction of vorticity for 3D Navier–Stokes flow, and then introduce recent results on the hyperbolic flow structure considered in the axisymmetric Navier–Stokes (or Euler) system.

Let us briefly look back at the history of the 3D Navier–Stokes equations. Modern regularity theory for solutions to the Navier–Stokes equations began with the works of Leray (1934) and Hopf (1951). They showed the existence of a weak solution $\boldsymbol{v}:[0, \infty) \times \mathbb{R}^3 \to \mathbb{R}^3$ lying in the class of $L^\infty(0, \infty; L^2(\mathbb{R}^3)) \cap L^2(0, \infty; \dot{H}^1(\mathbb{R}^3))$, which satisfies the global energy inequality, where $\dot{H}^1$ is a homogeneous Sobolev space with degree one.

After that, work by Prodi (1959), Serrin (1963) and Ladyzhenskaya (1967), and their joint efforts, led to the following Prodi–Serrin–Ladyzhenskaya criterion for the Leray–Hopf weak solutions.

THEOREM 1.1 (Prodi–Serrin–Ladyzhenskaya). *Let* $\boldsymbol{v} \in L^\infty(0, \infty; L^2(\mathbb{R}^3)) \cap L^2(0, \infty; \dot{H}^1(\mathbb{R}^3))$ *be a Leray–Hopf weak solution to (1.1), which also satisfies* $\boldsymbol{v} \in L^p(0, T; L^q(\mathbb{R}^3))$, *for some* p, q *satisfying* $2/p + 3/q = 1$, *with* $q > 3$. *Then, the solution* $\boldsymbol{v}$ *is smooth and unique on* $(0, T] \times \mathbb{R}^3$.

It is also worthwhile to mention that the exceptional case of $\boldsymbol{v} \in L^\infty(L^3)$ was finally established in the work of Escauriaza, Seregin & Sverak (2003). After the appearance of the Prodi–Serrin–Ladyzhenskaya criterion, many different regularity criteria for solutions to (1.1) were established by different researchers working on the regularity

theory of (1.1). For example, a regularity criterion along streamlines (characteristic curves) was constructed (see Chan & Yoneda 2012). Besides these, other important works have attracted much attention, such as Giga, Hsu & Maekawa (2014) – in which type I blow-up was excluded for solutions to (1.1) under a regularity condition on the direction of vorticity in the half space with no-slip boundary condition (see also Constantin & Fefferman (1993), which is the pioneering work in this field) – and Chen *et al.* (2009) and Koch *et al.* (2009) for axisymmetric solutions to (1.1) – the equation for the axisymmetric case can be rewritten as (1.3) – in the whole space. We now recall that a singularity of a Navier–Stokes solution $\boldsymbol{v}$ at a time T is called type I if

$$\sup_{\boldsymbol{x}} |\boldsymbol{v}(\boldsymbol{x}, t)| \leqslant \frac{C}{\sqrt{T-t}} \tag{1.2}$$

for some $C > 0$, where $\boldsymbol{x} = (x_1, x_2, z)$ denotes a space variable in Cartesian coordinates. If the singularity of $\boldsymbol{v}$ does not satisfy condition (1.2), then the singularity is called a type II singularity (refer to Koch *et al.* (2009) for the type of singularity). The axisymmetric Navier–Stokes equations are expressed as

$$\left.\begin{aligned} \partial_t u_r + u_r \partial_r u_r + u_z \partial_z u_r - \frac{{u_\theta}^2}{r} + \partial_r p &= \Delta u_r - \frac{u_r}{r^2}, \\ \partial_t u_\theta + u_r \partial_r u_\theta + u_z \partial_z u_\theta + \frac{u_r u_\theta}{r} &= \Delta u_\theta - \frac{u_\theta}{r^2}, \\ \partial_t u_z + u_r \partial_r u_z + u_z \partial_z u_z + \partial_z p &= \Delta u_z, \\ \frac{\partial_r (r u_r)}{r} + \partial_z u_z &= 0, \end{aligned}\right\} \tag{1.3}$$

where $u_r = u_r(r, z, t)$, $u_\theta = u_\theta(r, z, t)$, $u_z = u_z(r, z, t)$ and $\Delta = \partial_r^2 + (1/r)\partial_r + \partial_z^2$. The vector-valued function $\boldsymbol{v} := u_r e_r + u_\theta e_\theta + u_z e_z$ with $e_r := (1/\sqrt{x_1^2 + x_2^2})(x_1, x_2, 0)$, $e_\theta := (1/\sqrt{x_1^2 + x_2^2})(-x_2, x_1, 0)$ and $e_z = (0, 0, 1)$ represents the velocity of the fluid, and p is the pressure.

It is known that axisymmetric solutions for flows with no swirl (namely, $u_\theta \equiv 0$) have to be regular (see Ladyzhenskaya 1968; Ukhovskii & Iudovich 1968; Koch *et al.* 2009). On the other hand, Caffarelli, Kohn & Nirenberg (1982) showed that the axisymmetric Navier–Stokes solution could only blow up on the axis.

Choi *et al.* (2014) considered a one-dimensional (1D) transport equation with an additional variable that comes from the square of the swirl component u_θ of the velocity field in the 3D axisymmetric Euler flow. They showed that the transport equation can exhibit finite-time blow-up from smooth initial data by using an argument by contradiction, and they concluded that, in a 3D axisymmetric Euler flow, the best chance for possible singularity formation seemed to be at the hyperbolic saddle (see also Luo & Hou 2014). Indeed, the finite-time singularity numerically identified in Luo & Hou (2014) is located on the solid wall (lateral surface) of the cylinder, and the cylindrical domain considered by these authors is periodic in z (the axial direction), which means that no 'flat boundary' has been used to truncate the domain. Nevertheless, the special symmetries imposed in Luo & Hou (2014) forced the normal velocity component (u_z) of the flow to vanish on $z = 0$, effectively turning the plane into an 'impermeable wall' through which no fluid particle can pass. The 1D model considered in Choi *et al.* (2014) can be viewed as a projection of the 3D Euler equations onto the solid wall. It tried to model the hyperbolic saddle

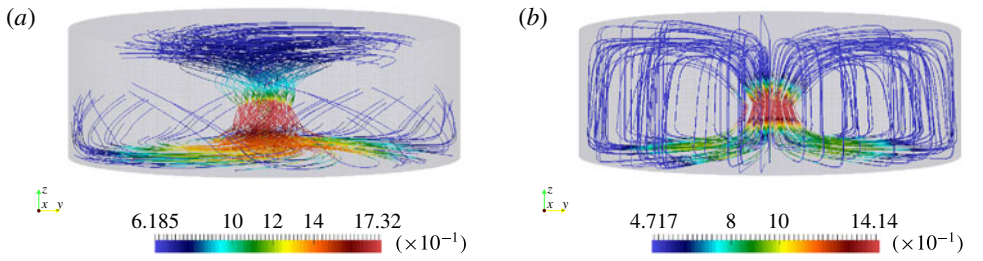

FIGURE 1. (Colour online) Initial data for $a = 1/8$: (*a*) swirl, and (*b*) no swirl.

lying at the intersection of the solid wall and the symmetry plane $z = 0$. On the other hand, Kang (2004) constructed a regularity theory. More precisely, suitable weak solutions of the 3D axisymmetric Navier–Stokes flow in a half space without swirl are Hölder-continuous up to the boundary except for the origin. His result suggests that, even in the case of the Navier–Stokes flow, the best possible position of singularity formation may be at the saddle point.

Although there are many fruitful results based on mathematical analysis, as mentioned above, it is not easy to locally analyse such fluid mechanics in order to go a step further mathematically. Thus, it would be effective to attempt a numerical approach.

Besides, from the above mathematical literature, the saddle point seems to be a key place and the hyperbolic flow with swirl might be a key structure. Actually, the swirl ratios are very significant in the research on tornadoes (see Wan & Ding 2005; Ishihara, Oh & Tokuyama 2011; Nolan 2012; Ishihara & Liu 2014). There are several methods for studying tornadoes. Although studies on real tornadoes that occur outdoors and simulated tornadoes in the laboratory are also important, numerical simulations provide a safe and cost-effective way to analyse the behaviour of tornadoes. We concentrate on numerical computation for the swirl case and the behaviour near the axis of symmetry (saddle point) at the boundary. From a mathematical point of view, the saddle point causes some type of unstabilizing effects. From the point of view of studies on tornadoes, the behaviour inside the core of a tornado (the centre region near the z-axis) is significant and might be very different compared to the behaviour outside the core. The behaviour near the ground (lower boundary) is also very significant for preventing damage caused by tornadoes. Our numerical result can be compared with the mathematical literature (especially regularity results; see Constantin & Fefferman 1993; Giga *et al.* 2014) and also with two-celled vortex structures in the research on tornadoes (especially numerical simulations). For more references, the reader should refer to Giga *et al.* (2014) for regularity results, to Luo & Hou (2014) for numerical studies of the Navier–Stokes and Euler equations, and to Nolan (2012) and Ishihara & Liu (2014) for studies on tornado-like vortices.

In the next section, we will describe the numerical computation used to observe the differences between the swirl case and the no-swirl case. We also show that the maximum value of $|\boldsymbol{v}|$ occurs at the place near the axis of symmetry (saddle point) and the boundary when the time approaches the critical turning point ($t = 0.35$ and $t = 1.0$) (refer to figures 1–7, especially figure 7).

2. Setting of the initial data and numerical results for the axisymmetric Navier–Stokes flow

In this section we set the initial data of the axisymmetric Navier–Stokes flow with a saddle point (with hyperbolic flow configuration). We compared two flows: the swirl ($u_\theta \not\equiv 0$) and no-swirl ($u_\theta \equiv 0$) cases. In our numerical computation, we used the cylindrical domain Ω,

$$\Omega := \left\{ \boldsymbol{x} = (x_1, x_2, z) \in \mathbb{R}^3 : -a < z < 4a,\ \sqrt{x_1^2 + x_2^2} < 1 \right\}, \tag{2.1}$$

and imposed the no-slip boundary condition,

$$\boldsymbol{v} = 0 \quad \text{on } \partial\Omega. \tag{2.2}$$

We set the initial data in the following manner (see also figure 1 and Remark 2.2). We let $\varphi(a, \epsilon, \sigma) = (a^2 + \epsilon)^\sigma$, and we set the initial velocity for the swirl case as follows:

$$u_z = \varphi(r, \epsilon_1, -\beta_1)\varphi(z, \epsilon_2, -\beta_2), \tag{2.3}$$
$$\rho = \varphi(r, \epsilon_3, -\beta_3)\varphi(z, \epsilon_4, \beta_4), \tag{2.4}$$
$$u_r = \mathrm{sign}(z)\rho u_z, \tag{2.5}$$
$$u_\theta = \varphi(r, \epsilon_5, -\beta_5)\varphi(z, \epsilon_6, -\beta_6), \tag{2.6}$$

where ϵ_i and β_i ($i = 1, 2, \ldots, 6$) are constants. In the following numerical calculation, we set all ϵ_i and β_i equal to 1. As for the no-swirl case, we only changed the term u_θ to zero.

Remark 2.1. By our setting of the initial data, the initial magnitude of velocity $|\boldsymbol{v}|$ at $(x_1, x_2, z) = (0, 0, 0)$ (we call this point the centre of the initial velocity) was larger than those at other places. The phenomena observed in this study were more clear when the centre of the initial velocity is close to the lower boundary (but not on the boundary). This is the reason for our choice of the computational domain Ω like (2.1) instead of a symmetric one. Please refer to the Appendix for a comparison between the behaviours of the two different centres.

Let $\tau > 0$ be a time increment of the computation and $h > 0$ a (representative) mesh size. We performed the computation by using a stabilized Lagrange–Galerkin (finite element) scheme (Notsu 2008; Notsu & Tabata 2008, 2015*a*,*b*) based on the idea

$$\frac{1}{\tau}\{\boldsymbol{v}^k(\boldsymbol{x}) - \boldsymbol{v}^{k-1}(\boldsymbol{x} - \boldsymbol{v}^{k-1}(\boldsymbol{x})\tau)\} - \frac{1}{Re}\Delta\boldsymbol{v}^k + \nabla p^k = 0, \tag{2.7a}$$
$$\nabla \cdot \boldsymbol{v}^k - \delta_0 h^2 \Delta p^k = 0, \tag{2.7b}$$

for $k = 1, 2, \ldots$, where $\boldsymbol{v}(\boldsymbol{x}, k\tau)$ is simply denoted by $\boldsymbol{v}^k(\boldsymbol{x})$, Re is the Reynolds number, and the stabilization parameter is set as $\delta_0 = 1$. We note that, under some conditions, the scheme has mathematical convergence properties of order $O(\tau + h)$ for the velocity in $H^1(\Omega)$ and for the pressure in $L^2(\Omega)$ and of order $O(\tau + h^2)$ for the velocity in $L^2(\Omega)$. The maximum, minimum and average mesh sizes were 1.88×10^{-2}, 1.48×10^{-3} and 8.95×10^{-3}, respectively, where the mesh size around the z-axis was smaller than that of the other part. The time increment was set as $\tau = 1.25 \times 10^{-2}$. In

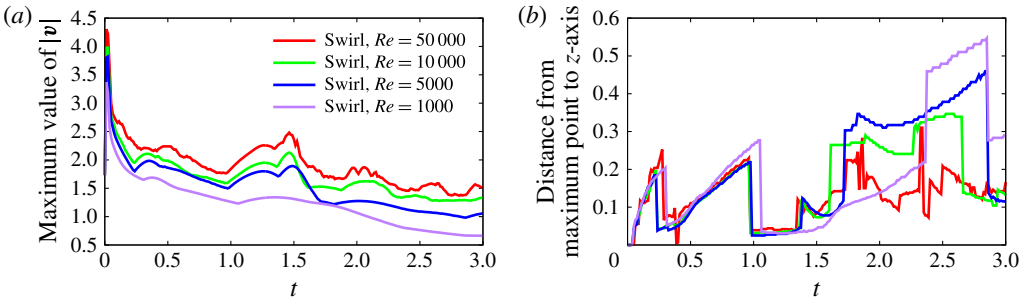

FIGURE 2. (Colour online) Graphs of (*a*) the maximum value of $|\boldsymbol{v}|$ versus t and (*b*) the distance from the maximum point of $|\boldsymbol{v}|$ to the z-axis versus t for the swirl case with Reynolds numbers 50 000 (red), 10 000 (green), 5000 (blue) and 1000 (purple).

the following sections, we show only the numerical results obtained using the mesh size and the time increment mentioned above, where the numerical results with a coarser mesh size and a larger time increment were qualitatively similar. Refer to the Appendix for the discussion on the dependence of the numerical results on the discretization parameters h and τ.

Remark 2.2. The initial velocities for the swirl and no-swirl cases did not satisfy the divergence-free and no-slip boundary conditions. The computational velocities after the first time step, however, satisfied both the conditions numerically, where the former condition was satisfied in the sense that (2.7*b*) held. The structure of the initial data is useful for observing the swirling flow. It is also reasonable to consider the initial data (2.3)–(2.6) as a pre-stage, and the velocities after the first time step as real initial velocity in the numerical computation. Although this construction of the initial data is useful for observing phenomena in numerical approaches before the construction of more smooth initial data, a more careful choice of the initial data is desirable for mathematical analysis.

Remark 2.3. The axial symmetry was not explicitly imposed in the 3D numerical computation by the stabilized Lagrange–Galerkin scheme, while the problem setting including the initial velocity had symmetry. We performed the computation in order to show the qualitative properties of the effect of swirl.

The figures show the numerical results obtained in our study for $a = 1/8$ and $Re =$ 1000, 5000, 10 000 and 50 000. Hereafter, we call the point at which the maximum value of $|\boldsymbol{v}|$ was attained as 'the maximum point of $|\boldsymbol{v}|$' and the cross-section $\{\boldsymbol{x} \in \Omega : x_1 = 0\}$ as simply 'the plane $x_1 = 0$'.

Figure 2 shows the graphs of maximum values of $|\boldsymbol{v}|$ versus time t and the distance from the maximum point of $|\boldsymbol{v}|$ to the z-axis versus time t for the swirl case, where four colours are used for the graphs of $Re = 50\,000$ (red), 10 000 (green), 5000 (blue) and 1000 (purple). Figure 3 expresses the corresponding graphs for the no-swirl case. From figures 2 and 3 we can see that different phenomena occur in the swirl and no-swirl cases. The typical phenomenon observed in the swirl case is the drastic changes of the distance from the maximum point of $|\boldsymbol{v}|$ to the z-axis at approximately $t = 0.35$ and 1.0, which is not observed in the no-swirl case. The difference becomes clearer for a higher-Reynolds-number flow. In order to understand the difference, we display

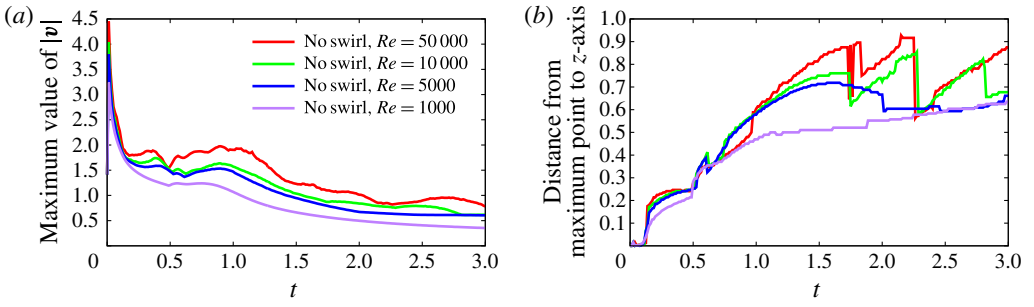

FIGURE 3. (Colour online) Graphs of (*a*) the maximum value of $|\boldsymbol{v}|$ versus t and (*b*) the distance from the maximum point of $|\boldsymbol{v}|$ to the z-axis versus t for the no-swirl case with Reynolds numbers 50 000 (red), 10 000 (green), 5000 (blue) and 1000 (purple).

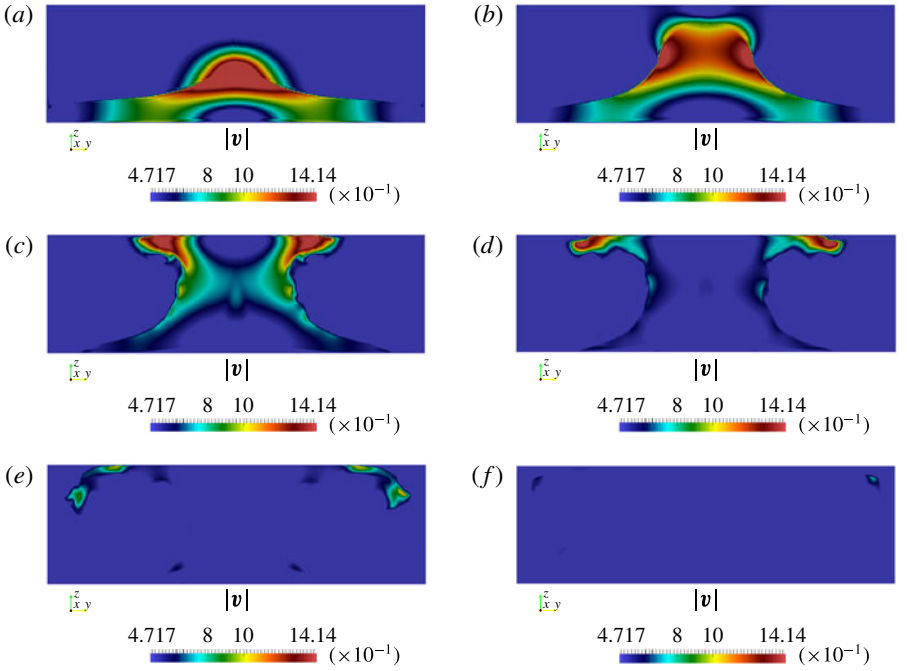

FIGURE 4. (Colour online) Time evolution of the velocity magnitude $|\boldsymbol{v}|$ on the plane $x_1 = 0$ for the no-swirl case with $Re = 50\,000$: $t = 0.1$ (*a*), 0.3 (*b*), 0.7 (*c*), 1.1 (*d*), 1.7 (*e*) and 3.0 (*f*).

time evolutions of velocity on the plane $x_1 = 0$ for both cases with $Re = 50\,000$ in figures 4–6. Figures 4 and 5 show the time evolutions of $|\boldsymbol{v}|$ on the plane for the no-swirl and swirl cases, respectively, and figure 6 exhibits the time evolution of the axial velocity u_z (z-component of $\boldsymbol{v}$) for the swirl case. They imply that the flow dissipates in a straightforward manner as t increases in the no-swirl case and that an interesting flow structure is observed near the z-axis in the swirl case.

From figures 2, 5 and 6 it can be observed that a downward flow arises near the z-axis at approximately $t = 0.3$, and the maximum value of $|\boldsymbol{v}|$ is attained near the z-axis and the lower boundary at approximately the same time ($t = 0.3$). In addition,

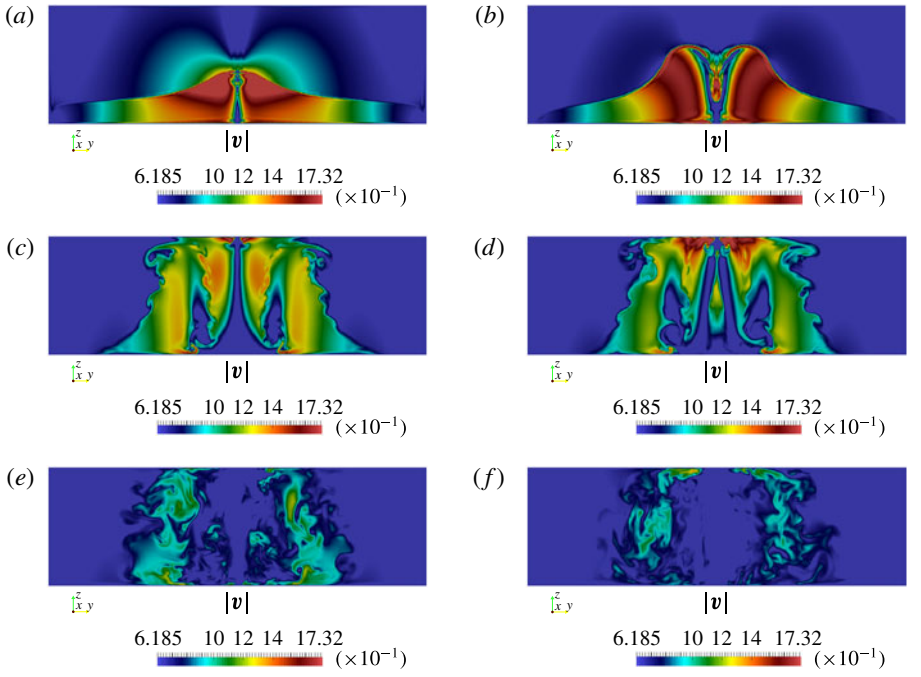

FIGURE 5. (Colour online) Time evolution of the velocity magnitude $|\boldsymbol{v}|$ on the plane $x_1 = 0$ for the swirl case with $Re = 50\,000$: $t = 0.1$ (*a*), 0.3 (*b*), 1.0 (*c*), 1.3 (*d*), 2.3 (*e*) and 3.0 (*f*).

a new upward flow arises near the z-axis at approximately $t = 1.3$, and the velocity attains its maximum value near the z-axis and the upper boundary at approximately the same time ($t = 1.3$).

Remark 2.4. The scale may be different in each figure. The red region represents a region of high magnitude.

3. Mathematical support for 'increasing velocity near the axis of symmetry and the lower boundary'

When unstabilizing effects are observed (such as increasing velocity in the time evolution), it is better to compare with stabilizing effects (such as regularity results mentioned in the introduction). The Giga–Hsu–Maekawa criterion (Giga *et al.* 2014, hereafter GHM criterion) was considered for the numerical computation described in the previous section. According to the GHM criterion (refer to (3.1) and also Giga *et al.* (2014, theorem 1.3)), type I blow-up solutions to (1.1) do not exist under a continuous alignment condition on the vorticity direction in the half space with no-slip boundary condition. More precisely, if the direction of vorticity can be controlled at places where the absolute value of the vorticity is large, the flow is regular. Conversely, if we can construct solutions that do not satisfy such continuous conditions at those places, there is a better possibility to determine the clue for possible blow-up solutions. As even in this study we could not construct a blow-up solution, this kind of thought might help us in explaining or predicting some phenomena with unstabilizing effects

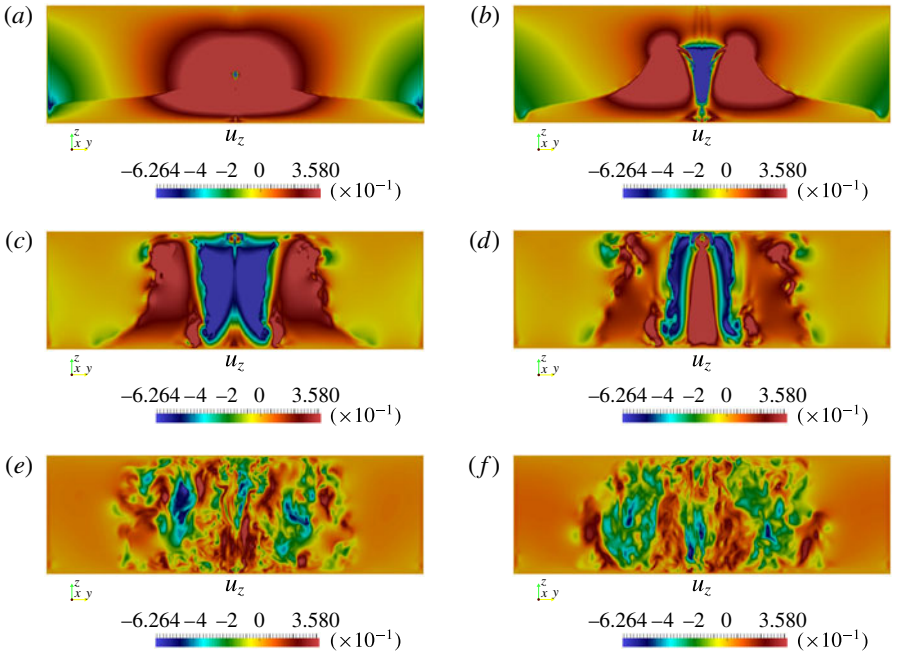

FIGURE 6. (Colour online) Time evolution of the axial velocity u_z on the plane $x_1 = 0$ in the swirl case with $Re = 50\,000$: $t = 0.1$ (*a*), 0.3 (*b*), 1.0 (*c*), 1.3 (*d*), 2.3 (*e*) and 3.0 (*f*). Note that the red and blue colours represent positive and negative values in this figure.

(such as the increasing velocity phenomena in this study). It should be noted that in our numerical computation, even if the cylindrical domain was used instead of the half space, the behaviour near the centre of the lower (and upper) boundary is expected to be similar to the boundary of the half space under the same boundary condition. Now we provide mathematical support for why the maximum value is increasing near the saddle point on the boundary. Let $\bar{\boldsymbol{u}} = u_\theta e_\theta + u_r e_r$ and $\bar{\boldsymbol{u}}^\perp = u_r e_\theta - u_\theta e_r$. We can calculate the vorticity on the boundary as $\boldsymbol{\omega} = \partial_z \bar{\boldsymbol{u}}^\perp$. Note that $\partial_z u_r(r, 0) \to 0$ as $r \to 0$ because of the symmetry. We can show that the direction of the vorticity $\boldsymbol{\omega}/|\boldsymbol{\omega}|$ is not continuous at the saddle point. In this case we need to assume $\partial_z u_\theta \neq 0$ (on the boundary) and $\partial_r u_\theta \neq 0$ (on the axis) near the saddle point. These non-zero conditions may express a 'shear flow effect by the swirl'. The vorticity along the axis is expressed as $\boldsymbol{\omega} = 2\partial_r u_\theta e_z$. Thus $\boldsymbol{\omega}/|\boldsymbol{\omega}|$ along the z-axis and on the boundary is not continuous. It breaks the following continuous alignment condition in the GHM criterion:

$$\left| \frac{\boldsymbol{\omega}}{|\boldsymbol{\omega}|}(t, \boldsymbol{x}) - \frac{\boldsymbol{\omega}}{|\boldsymbol{\omega}|}(t, \boldsymbol{y}) \right| \leqslant \rho(|\boldsymbol{x} - \boldsymbol{y}|), \tag{3.1}$$

where $\rho(|\boldsymbol{x} - \boldsymbol{y}|)$ is any modulus continuous function. However, this jump discontinuity in vorticity direction is irrelevant as far as phenomena with unstabilizing effects are concerned, since it takes place at a point where the vorticity $\boldsymbol{\omega}$ vanishes completely. Nevertheless, through numerical computations, we observe that there are high-vorticity regions near the saddle point and the boundary. We observe $|\boldsymbol{\omega}|$ and three components of $\boldsymbol{\xi} = \boldsymbol{\omega}/|\boldsymbol{\omega}|$ under a line that contains a point $(0, 0.05, -0.125)$ on the boundary and parallel to the z-axis at $t = 0.4$, as shown in figure 8 (figure 9 shows the case

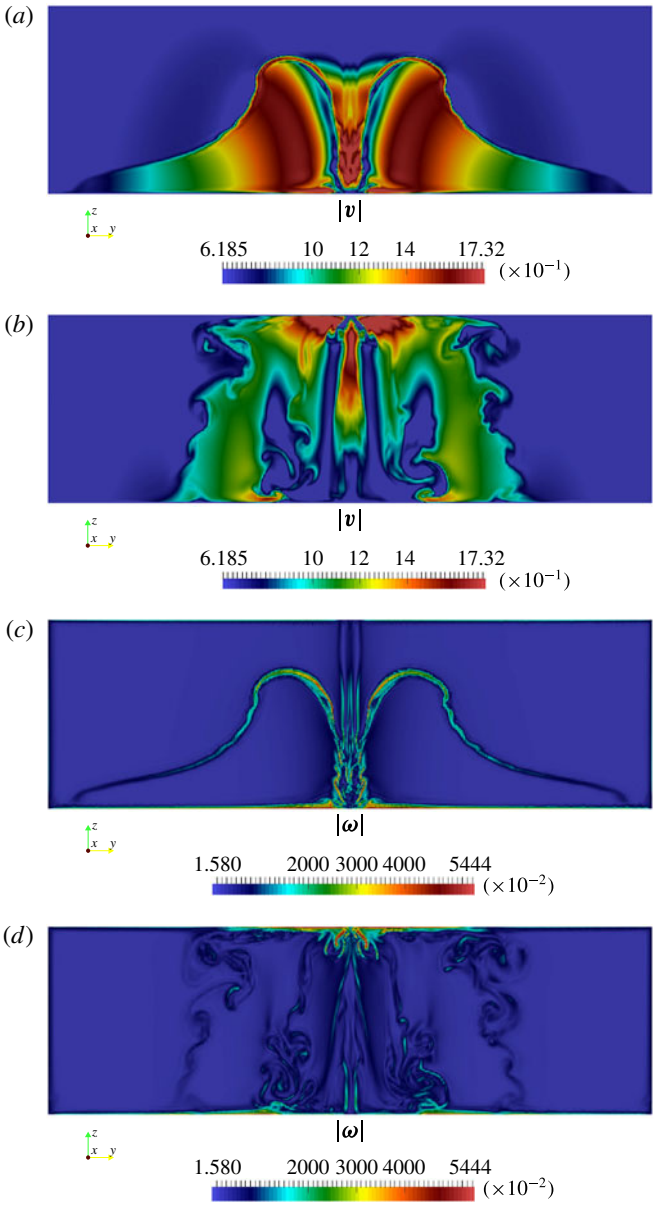

FIGURE 7. (Colour online) Contours on the plane $x_1 = 0$ of the velocity magnitude $|\boldsymbol{v}|$ at $t = 0.4$ (*a*) and $t = 1.4$ (*b*); and the vorticity magnitude $|\boldsymbol{\omega}|$ at $t = 0.4$ (*c*) and $t = 1.4$ (*d*) in the swirl case with $Re = 50\,000$.

where the line is parallel to the x_2-axis). The bottom axis in figure 8 represents the distance from the lower boundary, while the bottom axis in figure 9 represents the distance from the saddle point. It should be noted that the coordinate of the saddle point is $(0, 0, -0.125)$ and the axial velocity $u_z = 0$ on the boundary. At the point $(0, 0.05, -0.125)$ on the boundary, the magnitude of the vorticity $|\boldsymbol{\omega}|$ is 60, and it clearly attains the maximum value along the line in figure 8. Moreover $\boldsymbol{\omega}/|\boldsymbol{\omega}|$

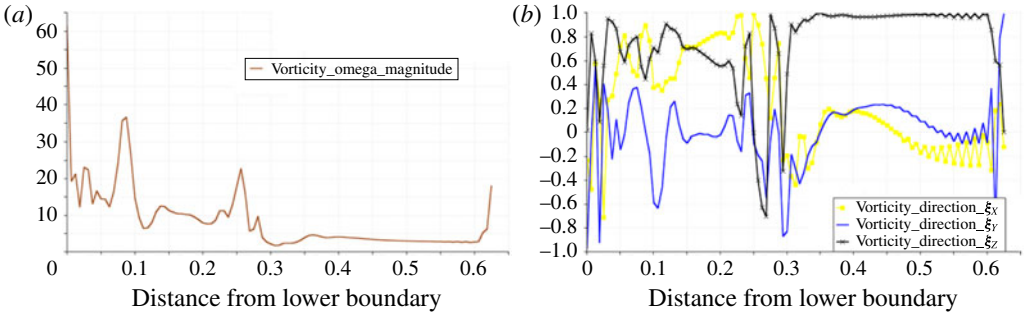

FIGURE 8. (Colour online) Graphs of $|\boldsymbol{\omega}|$ (a) and three components of $\boldsymbol{\xi}$ (b) at $t = 0.4$ on the line parallel to the z-axis through the point $(0, 0.05, -0.125)$.

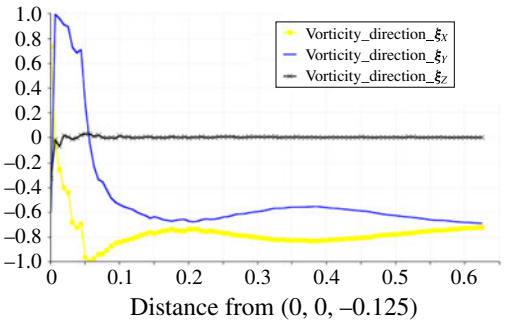

FIGURE 9. (Colour online) Graph of three components of $\boldsymbol{\xi}$ at $t = 0.4$ on the line parallel to the x_2-axis through the point $(0, 0.05, -0.125)$.

also changes drastically (highly oscillating) near the boundary (see figures 8 and 9). It shows some type of instability of $\boldsymbol{\xi}$ at the location where the magnitude of the vorticity is large.

4. Conclusion

From the literature, it is natural to consider that hyperbolic flow with swirl might be the key structure of flow and that a saddle point at the boundary might be the probable place for instability effects to occur near the no-slip flat boundary. We showed a clear structure of axisymmetric hyperbolic flow with swirl and observed the following phenomena that are distinctly different from those without swirl. (1) The distance between the maximum point of the velocity and the z-axis changed drastically at a specific time; we called it the turning point. (2) The velocity increased and attained its maximum value near the axis of symmetry and the boundary when the time was close to the turning point. The comparison of these results with studies on tornadoes might help in understanding the behaviour of the velocity of wind near the ground, which is very significant in research on tornadoes for reducing the damage caused by tornadoes or similar phenomena. (3) The downward flow near the z-axis was observed (refer to figure 6, the time evolution diagram). The downward wind inside the core of a real tornado was also observed in a two-celled vortex structure in the studies of numerical simulations for time-averaged velocity, as shown in Ishihara *et al.* (2011, figure 4*b*). By comparing our observation with studies on tornadoes, we might enhance our understanding about the behaviour inside the core of a tornado for

a high swirl ratio. Furthermore, we also observed the properties of vorticity and its directions (refer to § 3), on which there are only a few studies in the literature of the numerical simulations of tornadoes. Those phenomena might be clues for helping us understand the behaviour near the saddle point and near the boundary. Moreover, our numerical approach might be helpful for other boundary shapes and other equations related to fluid mechanics in future work. It might be useful for studies on tornadoes that arise or pass by different landforms instead of a flat plane.

Acknowledgements

First, we would like to thank the anonymous referees for carefully reading our manuscript and providing valuable comments especially on the literature (Luo & Hou 2014). We would like to extend our great gratitude to Professor N. Saito for giving us valuable suggestions on the construction of the initial data. We are also grateful to Professor V. Sverak for letting us know about interesting literature (Kang 2004; Choi *et al.* 2014). P.-Y.H. and T.Y. are supported by the 'Program to Promote the Tenure Track System' of the Ministry of Education, Culture, Sports, Science and Technology. Moreover, P.-Y.H. gratefully acknowledges the support of the Iwanami Fujukai Foundation. H.N. is supported by JSPS KAKENHI grant nos 26800091 and 24224004, by JSPS the Japanese–German Graduate Externship (Mathematical Fluid Dynamics) and by Waseda University Project research of Research Institute for Science and Engineering. T.Y. is partially supported by JSPS KAKENHI grant no. 25870004. The numerical computation is based on the Master's thesis of Mr H. Ishida at Hokkaido University in March 2014. This paper was developed during P.-Y.H.'s stay at Tokyo Institute of Technology. This research was supported by JST, CREST.

Appendix

Here, we present additional numerical results in order to show two observations: the first is that the dependence of the numerical results described in § 2 on the discretization parameters h and τ is qualitatively small; and the second observation describes the reason behind the choice of the range of z in Ω, i.e. $-a < z < 4a$.

First, we consider the former observation. We computed the no-swirl and swirl cases for $Re = 50\,000$, $10\,000$ and 5000 by using the stabilized Lagrange–Galerkin scheme with a coarse mesh and a large time increment. The maximum, minimum and average mesh sizes of the coarse mesh were 2.48×10^{-2}, 1.93×10^{-3} and 1.20×10^{-2}, respectively, where the strategy of the mesh generation was the same, i.e. the mesh size around the z-axis was smaller than that of the other part. The time increment was set as $\tau = 1.66 \times 10^{-2}$. Hereafter, we denote the numerical results described in § 2 as 'results A' and the numerical results obtained using the coarse mesh and the large time increment as 'results B'. We compared results B with results A for $Re = 50\,000$, $10\,000$ and 5000. Figure 10 shows graphs of maximum values of $|\boldsymbol{v}|$ versus t and the distance from the maximum point of $|\boldsymbol{v}|$ to the z-axis versus t in the swirl case for $Re = 50\,000$ (a,b), $10\,000$ (c,d) and 5000 (e,f), where the red and green colours are employed for results A and results B, respectively. Figure 11 displays the corresponding graphs for the no-swirl case for $Re = 50\,000$. From figures 10 and 11, we can see that the two graphs in each figure are qualitatively similar, while there is a quantitative difference. Here, the graphs for $Re = 10\,000$ and 5000 for the no-swirl case are omitted, since they are also qualitatively similar. We display additional information of results B in figure 12, which shows the contours of $|\boldsymbol{v}|$ (a,b)

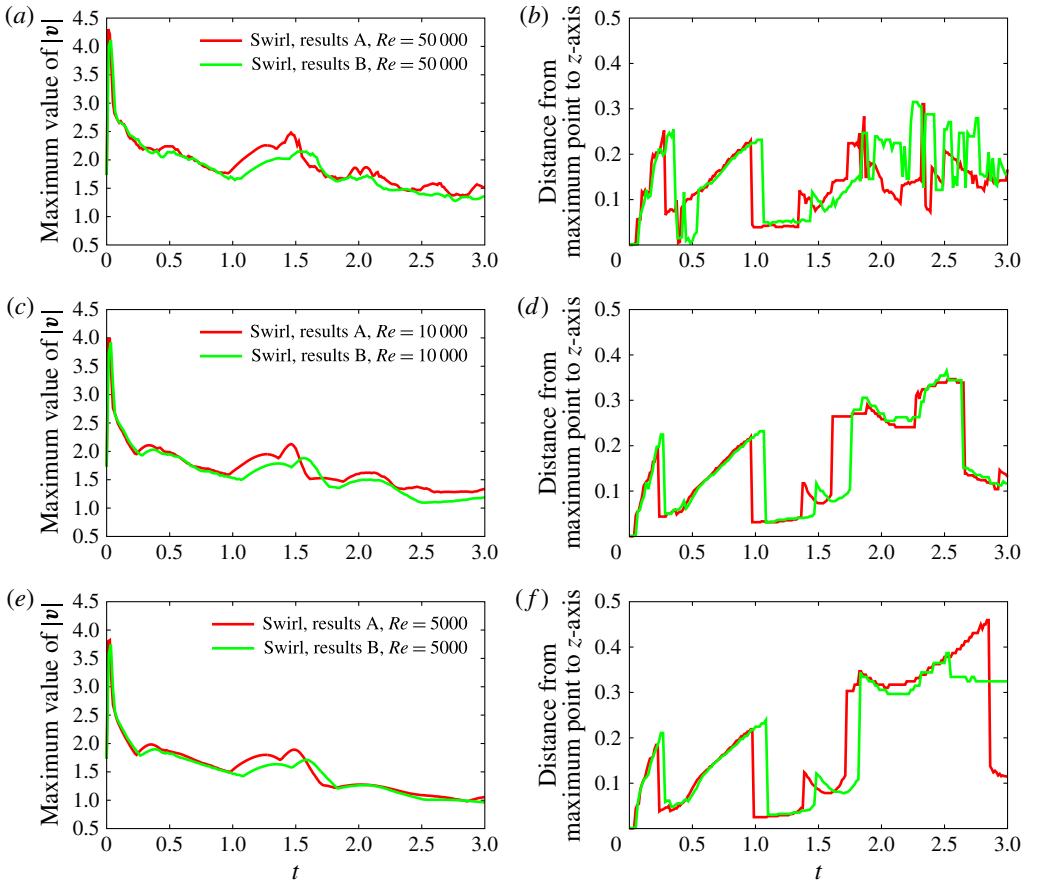

FIGURE 10. (Colour online) Graphs of (*a*,*c*,*e*) the maximum values of $|\boldsymbol{v}|$ versus t and (*b*,*d*,*f*) the distance from the maximum point of $|\boldsymbol{v}|$ to the z-axis versus t in the swirl case for $Re = 50\,000$ (*a*,*b*), $10\,000$ (*c*,*d*) and 5000 (*e*,*f*), where the red and green colours are employed for results A and results B, respectively.

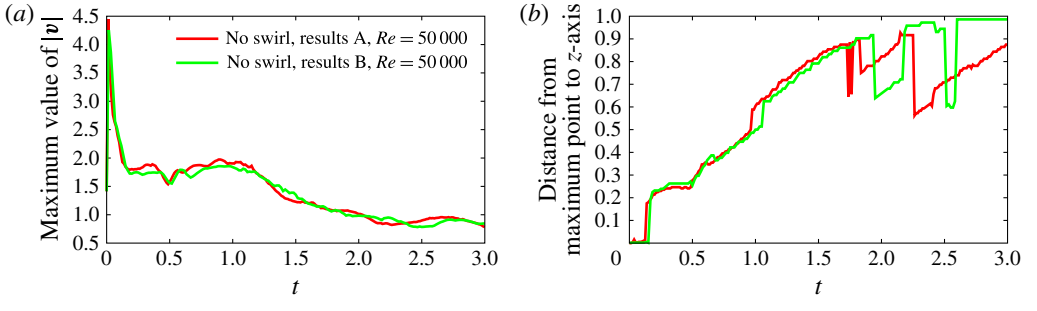

FIGURE 11. (Colour online) Graphs of (*a*) the maximum values of $|\boldsymbol{v}|$ versus t and (*b*) the distance from the maximum point of $|\boldsymbol{v}|$ to the z-axis versus t in the no-swirl case for $Re = 50\,000$, where the red and green colours are employed for results A and results B, respectively.

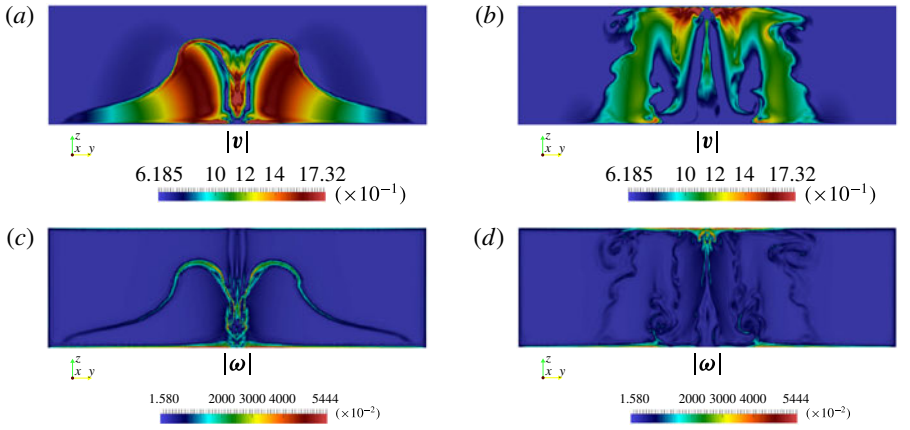

FIGURE 12. (Colour online) Contours on the plane $x_1 = 0$ of the velocity magnitude $|\boldsymbol{v}|$ (a,b) and the vorticity magnitude $|\boldsymbol{\omega}|$ (c,d) for the swirl case with $Re = 50\,000$ for results B, at $t = 0.4$ (a,c) and 1.4 (b,d).

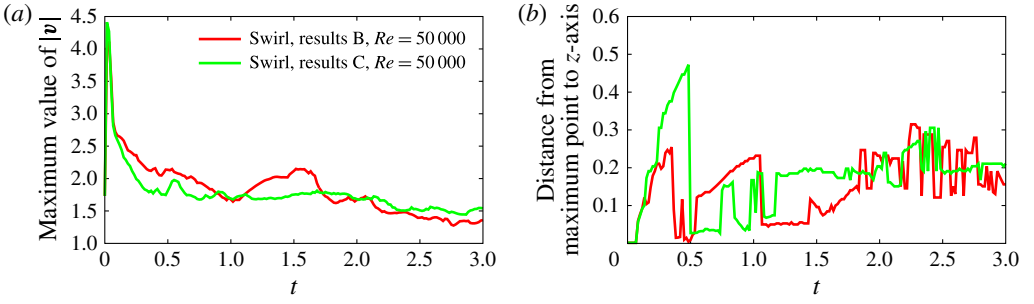

FIGURE 13. (Colour online) Graphs of (a) the maximum values of $|\boldsymbol{v}|$ versus t and (b) the distance from the maximum point of $|v|$ to the z-axis versus t in the swirl case for $Re = 50\,000$, where the red and green colours are employed for results B and results C, respectively.

and $|\boldsymbol{\omega}|$ (c,d) on the plane $x_1 = 0$ at $t = 0.4$ (a,c) and 1.4 (b,d), for $Re = 50\,000$ in the swirl case. By comparing figure 7 (results A) with figure 12 (results B) we can see that the behaviour of the two graphs is almost similar, although the magnitudes are slightly different. These results imply the former observation, i.e. the dependence of the numerical results in § 2 on the discretization parameters h and τ is qualitatively small.

Now we consider the latter observation. Let Ω' be a domain defined by $\Omega' := \{(x_1, x_2, z) \in \mathbb{R}^3 : -5a/2 < z < 5a/2,\ \sqrt{x_1^2 + x_2^2} < 1\}$. We note that the centres of Ω and Ω' are $(0, 0, 3a/2)$ and the origin, respectively. We computed the swirl case in the domain Ω' for $Re = 50\,000$ by using the stabilized Lagrange–Galerkin scheme with a coarse mesh and a large time increment, where the initial data were set by the same functions in (2.3)–(2.6). The mesh sizes and the time increment were the same as those used in results B. (The mesh was generated by a translation of the mesh for results B.) We denote the numerical results as 'results C'. We compare results C with results B in figure 13, which shows the graphs of the maximum values of $|\boldsymbol{v}|$ versus

t and the distance from the maximum point of $|\boldsymbol{v}|$ to the z-axis versus t in the swirl case for $Re = 50\,000$, where the red and green colours are employed for results B and results C, respectively. It is observed that the 'increasing velocity phenomenon' in results B is clearer than that in results C, and that drastic changes of the distance from the maximum point of $|\boldsymbol{v}|$ to the z-axis are observed in both the results. Hence, Ω is better than Ω' in order to observe both the 'increasing velocity phenomenon' and 'drastic changes'. These results explain the reason behind the choice of the range of z in Ω, $-a < z < 4a$.

REFERENCES

BOURGAIN, J. & LI, D. 2015*a* Strong ill-posedness of the incompressible Euler equations in borderline Sobolev spaces. *Invent. Math.* **201**, 97–157.

BOURGAIN, J. & LI, D. 2015*b* Strong illposedness of the incompressible Euler equation in integer C^m spaces. *Geom. Funct. Anal.* **25**, 1–86.

CAFFARELLI, L., KOHN, R. & NIRENBERG, L. 1982 Partial regularity of suitable weak solutions of the Navier–Stokes equations. *Commun. Pure Appl. Maths* **35**, 771–831.

CHAN, C.-H. & YONEDA, T. 2012 On possible isolated blow-up phenomena and regularity criterion of the 3D Navier–Stokes equation along the streamlines. *Meth. Appl. Anal.* **19**, 211–242.

CHEN, C.-C., STRAIN, R. M., TSAI, T.-P. & YAU, H.-T. 2009 Lower bounds on the blow-up rate of the axisymmetric Navier–Stokes equations. II. *Commun. Part. Diff. Equ.* **34**, 203–232.

CHOI, K., HOU, T., KISELEV, A., LUO, G., SVERAK, V. & YAO, Y. 2014 On the finite-time blowup of a 1D model for the 3D axisymmetric Euler equations. Preprint, arXiv:1407.4776.

CONSTANTIN, P. & FEFFERMAN, C. 1993 Direction of vorticity and the problem of global regularity for the Navier–Stokes equations. *Indiana Univ. Math. J.* **42**, 775–789.

ELGINDI, T. & MASMOUDI, N. 2014 L^∞ ill-posedness for a class of equations arising in hydrodynamics. Preprint, arXiv:1405.2478 [math.AP].

ESCAURIAZA, L., SEREGIN, G. A. & SVERAK, V. 2003 $L_{3,\infty}$-solutions of Navier–Stokes equations and backward uniqueness. *Usp. Mat. Nauk* **58**, 3–44.

GIGA, Y., HSU, P.-Y. & MAEKAWA, Y. 2014 A Liouville theorem for the planar Navier–Stokes equations with the no-slip boundary condition and its application to a geometric regularity criterion. *Commun. Part. Diff. Equ.* **39** (10), 1906–1935.

HOPF, E. 1951 Uber die Anfangswertaufgabe fur die hydrodynamischen Grundgleichungen. *Math. Nachr.* **4**, 213–231.

ISHIHARA, T. & LIU, Z. 2014 Numerical study on dynamics of a tornado-like vortex with touching down by using the LES turbulent model. *Wind Struct.* **19**, 89–111.

ISHIHARA, T., OH, S. & TOKUYAMA, Y. 2011 Numerical study on flow fields of tornado-like vortices using the LES turbulence model. *J. Wind Engng Ind. Aerodyn.* **99**, 239–248.

ITOH, T., MIURA, H. & YONEDA, T. 2014 Remark on single exponential bound of the vorticity gradient for the two-dimensional Euler flow around a corner. *J. Math. Fluid Mech.* (in press).

KANG, K. 2004 Regularity of axially symmetric flows in a half-space in three dimensions. *SIAM J. Math. Anal.* **35**, 1636–1643.

KISELEV, A. & SVERAK, V. 2014 Small scale creation for solutions of the incompressible two dimensional Euler equation. *Ann. Maths* **180**, 1205–1220.

KISELEV, A. & ZLATOS, A. 2015 Blow up for the 2D Euler equation on some bounded domains. *J. Differ. Equ.* **259** (7), 3490–3494.

KOCH, G., NADIRASHVILI, N., SEREGIN, G. & SVERAK, V. 2009 Liouville theorems for the Navier–Stokes equations and applications. *Acta Math.* **203** (1), 83–105.

LADYZHENSKAYA, O. A. 1967 Uniqueness and smoothness of generalized solutions of Navier–Stokes equations. *Zap. Nauchn. Sem. Leningrad. Otdel. Mat. Inst. Steklov. (LOMI)* **5**, 169–185.

LADYZHENSKAYA, O. A. 1968 On the unique global solvability to the Cauchy problem for the Navier–Stokes equations in the presence of the axial symmetry. *Zap. Nauchn. Sem. Leningrad. Otdel. Mat. Inst. Steklov. (LOMI)* **7**, 155–177.

LERAY, J. 1934 Sur le mouvement d'un liquide visqueux emplissant l'espace. *Acta Math.* **63**, 193–248.

LUO, G. & HOU, T. Y. 2014 Potentially singular solutions of the 3D incompressible Euler equations. *Proc. Natl Acad. Sci. USA* **111** (36), 12968–12973.

NOLAN, D. S. 2012 Three-dimensional instabilities in tornado-like vortices with secondary circulations. *J. Fluid Mech.* **711**, 61–100.

NOTSU, H. 2008 Numerical computations of cavity flow problems by a pressure stabilized characteristic-curve finite element scheme. *Trans. Japan. Soc. Comput. Engng Sci.* **2008**, 20080032.

NOTSU, H. & TABATA, M. 2008 A combined finite element scheme with a pressure stabilization and a characteristic-curve method for the Navier–Stokes equations (in Japanese). *Trans. Japan. Soc. Ind. Appl. Maths* No. 18, 427–445.

NOTSU, H. & TABATA, M. 2015*a* Error estimates of a pressure-stabilized characteristics finite element scheme for the Oseen equations. *J. Sci. Comput.* **65**, 940–955.

NOTSU, H. & TABATA, M. 2015*b* Error estimates of a stabilized Lagrange–Galerkin scheme for the Navier–Stokes equations. *ESAIM: Proc. M2AN* **50**, 361–380.

PRODI, G. 1959 Un teorema di unicita per le equazioni di Navier–Stokes. *Ann. Mat. Pura Appl.* **48**, 173–182.

SERRIN, J. 1963 The initial value problem for the Navier–Stokes equations. In *Nonlinear Problems (Proc. Symp., Madison, WI)*, University of Wisconsin Press.

UKHOVSKII, M. R. & IUDOVICH, V. I. 1968 Axially symmetric flows of ideal and viscous fluids filling the whole space. *Z. Angew. Math. Mech.* **32**, 52–61.

WAN, J. W. L. & DING, X. 2005 Physically-based simulation of tornadoes. In *Proceedings of the Second International Conference on Virtual Reality Interaction and Physical Simulation, ISTI-CNR, Pisa, Italy*.

XU, X. 2014 Fast growth of the vorticity gradient in symmetric smooth domains for 2D incompressible ideal flow. *J. Math. Anal. Appl.* (in press); doi:10.1016/j.jmaa.2016.02.066.